ENHANCEMENT OF PRESCRIBED WAKE CODES WITH A CFD-BASED MODEL OF THE FUSELAGE-INDUCED VELOCITIES

Berend G. van der Wall
German Aerospace Center
38108 Braunschweig, Germany
berend.vanderwall@dlr.de

André Bauknecht
German Aerospace Center
37073 Göttingen, Germany
andre.bauknecht@dlr.de

Sung N. Jung, Young H. You
Konkuk University
143-701 Seoul, Korea
snjung@konkuk.ac.kr

Abstract

An analytical formulation of the induced velocities caused by the fuselage shell of the HART II wind tunnel model in the vicinity of the rotor is derived from computational fluid dynamics (CFD) velocity data. The analytical induced velocity model can directly be used to account for the inflow at the blade elements and also allows for analytical integration to compute the associated displacements of rotor blade tip vortices convecting downstream through this velocity field. The implementation is demonstrated at the example of the rotor simulation program S4 of the German Aerospace Center (DLR) in Braunschweig. The model's influence on the major flow field variables around the rotor disk and the wake trajectory is demonstrated. Since the method is generic it is anticipated that the effect of any kind of fuselage can be accounted for this way and it may be used within any comprehensive code, prescribed wake code, and even free-wake codes.

Nomenclature

A, B	effective begin and end of airfoiled section, made non-dimensional by R
A_0	magnitude
c	rotor blade chord, m
$C_{l\alpha}$	lift curve slope
C_T	thrust coefficient, $= T/(\rho\pi R^2(\Omega R)^2)$
f_A, f_x, f_z	form parameters of shape functions
M	Mach number
M_β	aerodynamic moment about flap hinge, Nm
N_b	number of blades
P	rotor power, kW
r	non-dimensional rotor radius
R	rotor radius, m
T	rotor thrust, N
S_A, S_x, S_y	shape functions for amplitude, in x- and in y-direction
v_{if}	fuselage-induced velocity, m/s
V_T, V_P	velocities tangential and perpendicular to the hub plane at the blade element, m/s
V_∞	flight speed, m/s
x, y, z	hub fixed coordinates, m
x_0, z_0	position of maximum induced velocities, m
z_v	vortex position, m
z_R, z_F	vortex position due to rotor- and fuselage-induced velocities, m
α, α_a	fuselage and blade element incidence, deg
Θ	blade element pitch angle, deg
$\Theta_0, \Theta_C, \Theta_S$	collective, lateral and longitudinal cyclic control angle, deg
λ_{if}	fuselage-induced inflow ratio, = v_{if}/V_∞
μ	advance ratio, $= V_\infty/\Omega R$
ρ	air density, kg/m³
σ	solidity, $= N_b c/(\pi R)$
ψ	rotor blade azimuth, deg
Ω	rotor rotational speed, rad/s

1. INTRODUCTION

Rotorcraft interactional aerodynamics has been one of the key research concerns for the design, performance, handling qualities, vibration, and aeroacoustic radiation [1]-[3]. The interaction occurs between the sublevel components such as the rotor, hub, fuselage, empennage, tail stabilizers, and tail rotor. The effects are essentially nonlinear and dependent on the flight conditions and thrust levels. Because of the general trends for higher disk loadings of the rotor and advanced operational requirements (e.g. smaller clearance and higher transportability) in modern helicopter designs, the interaction phenomena have become more problematic. During the last decades, a large volume of research has been conducted to identify the sources of the problem which led to closer understanding of the interaction mechanisms and advancing the prediction capability of complete helicopter configurations. The studies can be categorized as purely experimental or experimental-cum-theoretical work [4]-[12], simple analytical or numerical work that uses simplified aerodynamic and structural models [13]-[22], and computationally more involved work that directly solves Euler or Navier-Stokes equations for the rotorcraft flow field [23]-[32].

Leishman and his associates [4], [5], [7], [11] investigated the interference effects for a scaled rotor/body model in a wind tunnel by varying the flight speeds and shaft orientation angles while fixing the distance between the rotor and fuselage. They used structurally rigid blades to simplify the investigation. Both steady and unsteady aerodynamic loads were measured using pressure

transducers distributed over the fuselage surface. In addition to the combined rotor/body configuration, either the isolated rotor or the isolated fuselage case was tested to determine the interaction effects separately. The interaction effects were found to be significant in hover and low speed forward flight. The rotor generated a download on the fuselage due to the downwash of the rotor and, in reverse, the fuselage affected the rotor by substantially increasing the thrust. After re-trimming to the isolated rotor thrust a reduction of the rotor power was observed: the fuselage acted similar to ground effect. Unsteady pressure fluctuations on the body were detected at blade passage frequencies. A lifting-line blade element theory of the rotor was coupled with a source-panel model of the body to provide the numerical predictions of the rotor/body interaction analysis. A prescribed wake model was used to calculate the local induced velocities of the rotor. Fair correlation between measured and computed surface pressures was obtained with the simple analysis.

The conventional analytical model for the interaction phenomena typically used a lifting-line aerodynamic model with rigid [11], [16], [20] or elastic [13]-[15] blade representation, a prescribed (vortex rings) [11], [14], [18] or free wake [16], [20] representation of the vortex wake, along with a source panel fuselage model. These first generation models have been evolved to more refined analytical models such as Wachspress et al. [21] and Kenyon and Brown [22]. The former used a fast vortex/fast panel method to predict the rotor/body/wake problem under the limitation of the non-viscous flow assumption. This obvious limitation was overcome in the latter approach by introducing the vorticity transport model developed based on the solutions of the Navier-Stokes equations in vorticity-velocity form. A remarkable feature of this approach was a vortex wake computation that showed little numerical dissipation with less computational requirements as compared with the conventional CFD (Computational Fluid Dynamics) approaches. Despite the advantage in wake preserving characteristic of the method, some controversies surfaced especially with regard to a grid convergence problem [23].

Thanks to the notable growth of computer hardware capabilities, the CFD-based methods such as RANS (Reynolds-Averaged Navier-Stokes) solvers have become realized as one of the most powerful tools to tackle the rotorcraft aerodynamic interaction problem. Nam et al. [24] used Euler simulations on unstructured meshes to estimate the interactional aerodynamic features of rotor/body coupled configurations. A sliding mesh algorithm was adopted to deal with the rotational motion of the rotor in relation to the non-rotating rectangular grids. The correlation results showed reasonable agreements with the wind tunnel measurement data with substantial deviations of the rotor-induced velocities and static pressures near tip vortex impingement locations. Neglecting the viscous effects was attributed to cause the discrepancy. The most up-to-date CFD approaches used an unsteady RANS solver combined with a structured [25], [28], [30], [33] or an unstructured [32] overset grid system. The viscous boundary layers were taken into account naturally with proper choice of the turbulence modeling. The recent studies on the aerodynamic interaction include a complete helicopter configuration including the tail rotor [33].

Even though the direct usage of CFD is viable and sometimes desired in predicting the complicated interaction behavior accurately, it is still computationally expensive and prohibitive especially for cases within the preliminary design stage of a rotorcraft. Whereas the conventional approach based on lifting-line theory with prescribed or free vortex wake model lacks the critical accuracy required in the rigorous evaluation of various physical phenomena, these simplified methods are advantageous particularly in terms of the computational efficiency. It is estimated for an isolated rotor case that the computational costs would be reduced by six orders of magnitude compared to the CFD counterpart method [34]. With a view on the aforementioned aspects in the rotor/fuselage interaction problems, an alternative and computationally more efficient way can be reached combining the prescribed wake modeling with the state-of-the-art CFD approach. In the context of the present research, a RANS CFD solver computes the flow fields around a rotor induced by a fuselage and these CFD results are then fed into the lifting-line method for both efficiency and accuracy requirements.

For the calculation of loads and power on a rotary-wing aircraft, information about the interaction between the unsteady aerodynamics and the structural mechanics of the rotor system is required. The entire regime of induced velocities has to be taken into account too, especially the self-induced velocities of the rotor system. Although the rotor flow dominates the overall balance, other influences - particularly the interaction with the helicopter fuselage - have to be considered as well to fully describe the velocity field resulting in the rotor disk [35] shown schematically in Fig. 1.

The proximity of a helicopter fuselage to the lifting rotor is a known source of vibration due to aerodynamic interactions between both, especially due to the velocities caused by the displacement

flow of the fuselage body within the rotor disk that represent an unsteady variation of the rotor blade section angle of attack and the local dynamic pressure. The short distance to the rotor plane leads to two separate fuselage interaction effects that have to be distinguished. The downwash of the rotor and consequently the rotor wake vortices experience a displacement due to the presence of the fuselage. This effect is persisting in all flight conditions, while the rotor downwash itself becomes less important with increasing flight speed since it is proportional to the inverse of it. In hover, the fuselage partially blocks the induced flow field of the rotor. In forward flight, the fuselage causes an inflow increasing proportional with the flight speed, which affects the total fuselage-induced velocity field of the rotor.

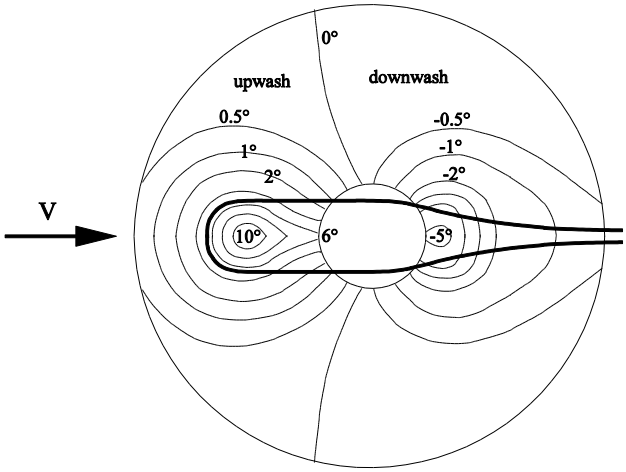

Fig. 1: Distribution of flow deflection angles in the plane of the rotor due to the fuselage.

The mutual effects of rotor-fuselage and fuselage-rotor interactions are highlighted in [36]: “The problem of correctly modeling aerodynamic interference in a rotorcraft is as much art as it is science. The downwash from a rotor impinges on the fuselage, striking it almost normally. With forward speed, the wake decreases in strength and moves toward the tail. The fuselage itself also decelerates or redirects the moving air, influencing all other bodies attached to it. As the fuselage plows through the air, the air above it is pushed out of the way. The air also is retarded directly in front of the fuselage, but accelerated in the x direction over the top of the fuselage. A potential flow model of the fuselage is one method to estimate the effect.”

The present work focuses on this second effect and especially its application to the rotor simulation program S4, which has been developed at the German Aerospace Center (DLR) in Braunschweig [37]-[38]. S4 is a prescribed-wake code, capable of calculating loads, rotor deformations, and flow field variables in the rotor plane, and vortex trajectories in its wake. In the previous version of the program, fuselage effects could be considered for two DLR test rigs (ROTOS and ROTEST). The induced velocity fields of their fairings have been calculated in the past using an incompressible panel method and are represented in S4 as analytical functions [39]. To expand the possibilities of the rotor simulation program, the present work aims at implementing a CFD-based induced velocity field of the HART II test stand as a third fuselage option.

The simulations were carried out by Konkuk University within a Memorandum of Understanding with DLR using the CFD solver KFLOW [40], [41] while DLR performed the engineering analysis and model identification. Note that the fuselage surface data are available through the HART II International Workshop [42].

2. THEORETICAL APPROACH

2.1. Fourier Representation of Fuselage-Induced Velocities

Using blade element theory a rough estimate of the amount of additional thrust due to the presence of a fuselage is derived next. A non-lifting untwisted, rectangular rotor blade, that - without a fuselage - will generate zero thrust, may be subjected to the induced velocity field of a fuselage below it. The latter was estimated by a CFD computation (see section 3) of an isolated fuselage as used during the HART wind tunnel tests and results are shown in Fig. 2 (a) for a fuselage angle of attack of $\alpha = 0°$ and zero sideslip in a plane $z/R = 0$ (= rotor hub plane: origin in the hub center, x downstream, y starboard, z up).

Since these velocities are proportional to flight speed, the non-dimensional distribution is referenced to the free-stream velocity V_∞ and is thus independent of flight speed. The range of helicopter flight speeds remains below a Mach number of $M = 0.3$ and compressibility effects can thus be ignored. It can be seen that the distribution is symmetric with respect to the plane $y/R = 0$, which is due to the lateral symmetry of the fuselage. The maximum and minimum peaks are in the range of 10% of the flight speed, asymptotically decreasing to small values for outer radii. In the front of the disk an upwash area is visible (green and blue areas) and in the rear a downwash area (yellow and red areas).

A downwash velocity is defined as positive as is usual in rotor aerodynamics. The periodicity suggests a Fourier representation in azimuth and due to the lateral symmetry only Cosine terms are present, aside a mean value, which represents the Cosine of $0/rev$ and which is shown in Fig. 2 (b), together with the Cosine of the 1 and $2/rev$. Therefore, with r as non-dimensional radial

coordinate and for a given fuselage angle of attack its induced velocities within the rotor plane may be given as

$$\frac{v_{if}}{V_\infty} = \lambda_{if}(r,\psi) = \sum_{n=0}^{\infty} \lambda_{ifn}(r)\cos(n\psi) \tag{1.1}$$

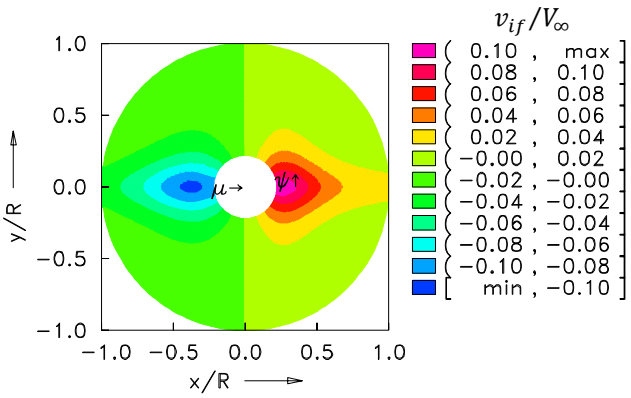

(a) Distribution in the rotor disk

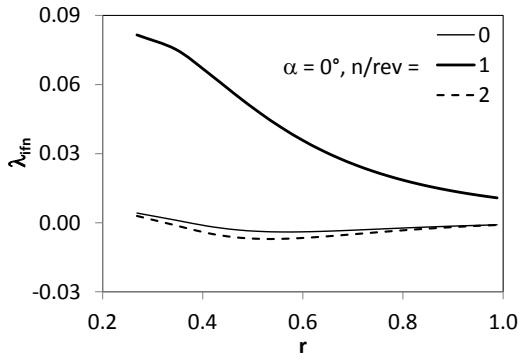

(b) Radial distribution of harmonics 0, 1, 2

Fig. 2: HART II fuselage-induced velocities normal to the rotor disk for α = 0°in the plane z/R = 0.

They are referenced to the flight speed, but within the rotor environment need to be referenced to the blade tip speed. This results in a multiplication by the advance ratio $\mu = V_\infty / (\Omega R)$, where ΩR is the tip speed. Fig. 2 (b) also suggests that the radial distributions of the n/rev induced velocities may be represented by a polynomial of N-th order:

$$\lambda_{if\,0}(r) = \sum_{n=0}^{N} c_{n0} r^n \tag{1.2}$$

$N = 3$ will be sufficient to represent the curves of Fig. 2 (b) with good accuracy.

2.2. Impact on Rotor Thrust

Application of blade element theory requires the non-dimensional tangential (V_T) and normal (V_P) velocities acting at a blade element in forward flight and the local angle of attack α_a caused by these. They are defined by the pilot's cyclic pitch controls Θ_C, Θ_S and by the fuselage-induced inflow ratio (normal velocities are defined as positive down).

$$\begin{aligned} V_T &= \Omega R(r + \mu\sin\psi) \\ V_P &= \Omega R \mu \lambda_{if}(r,\psi) \\ \alpha_a &= \Theta - \arctan\left(V_P/V_T\right) \\ &\approx \Theta_C\cos\psi + \Theta_S\sin\psi - V_P/V_T \end{aligned} \tag{1.3}$$

A collective control as well as blade twist are ignored (or kept fixed) since the increase of thrust relative to some constant value is of interest, for example relative to zero thrust of the isolated rotor as given here.

The cyclic controls, however, are retained since they will be used to compensate for the hub moments that also will develop due to the fuselage influence. The maximum positive angle of attack caused by the extreme values of fuselage-induced velocities in the front of the disk extracted from Fig. 2 (a) are found at $y = 0$ or $\psi = 0°, 180°$. Thus:

$$\alpha_{max} = -\mu\frac{\lambda_{max}}{r(\lambda_{max})} = -\mu\frac{-0.1}{0.5} = 0.2\mu \tag{1.4}$$

For a high advance ratio of $\mu = 0.5$ this amounts to $\alpha_{max} = 5.8°$, a considerable value. The differential thrust of a N-bladed rotor generated by a blade element of chord c and length $R\,dr$ in air with density ρ and a lift curve slope $C_{l\alpha}$ is

$$dT = N\frac{\rho}{2}V_T^2 cRC_{l\alpha}\alpha_a\,dr \tag{1.5}$$

In non-dimensional form this is referenced to $\rho\pi R^2(\Omega R)^2$, and after substituting $C_{l\alpha} = 2\pi$ from 2D incompressible flat plate theory the differential thrust coefficient becomes (with solidity $\sigma = Nc/(\pi R)$ of a rectangular blade)

$$\begin{aligned} dC_T = \pi\sigma\Big[&(r+\mu\sin\psi)^2(\Theta_C\cos\psi + \Theta_S\sin\psi) \\ &-(r+\mu\sin\psi)\mu\sum_{n=0}^{\infty}\lambda_{ifn}(r)\cos(n\psi)\Big]dr \end{aligned} \tag{1.6}$$

The total thrust coefficient is obtained after averaging over the azimuth and integration along the span. The blade loading is then computed by referencing to the rotor solidity and integrating over the lifting part of the blade, i.e., from the effective root cut-out A to the effective blade tip B (for simplicity this may also be set to $A = 0$ and $B = 1$).

$$\begin{aligned} \Delta C_T &= \frac{1}{2\pi}\int_0^{2\pi}\int_A^B dC_T\,d\psi \\ \frac{\Delta C_T}{\sigma} &= \frac{1}{2}\int_0^{2\pi}\int_A^B(\Theta_C\cos\psi + \Theta_S\sin\psi)\times \\ &\quad\left[r^2 + 2r\mu\sin\psi + \frac{\mu^2}{2}(1-\cos 2\psi)\right]dr\,d\psi \\ &\quad -\frac{\mu}{2}\int_0^{2\pi}\int_A^B(r+\mu\sin\psi)\sum_{n=0}^{\infty}\lambda_{ifn}(r)\cos(n\psi)\,dr\,d\psi \end{aligned} \tag{1.7}$$

All harmonic terms $\int_0^{2\pi} \sin n\psi \, d\psi = \int_0^{2\pi} \cos n\psi \, d\psi = 0$ and the only remaining part is

$$\frac{\Delta C_T}{\sigma} = \mu\pi \int_A^B \left[r\Theta_S - r\lambda_{if\,0}(r) \right] dr \quad (1.8)$$

The radial distribution of the mean part of the fuselage-induced velocity of Fig. 2 (a) is shown in Fig. 2 (b) and can well be approximated by a polynomial in the radial coordinate as given before, such that

$$\frac{\Delta C_T}{\sigma} = \mu\pi \left(\Theta_S \frac{B^2 - A^2}{2} - \sum_{n=0}^{N} c_{n0} \frac{B^{n+2} - A^{n+2}}{n+2} \right) \quad (1.9)$$

The coefficients are given in Table 1 for the mean of the radial distribution $(\lambda_{if\,0})$ and for $\alpha = 0°$, and also for the amplitude distributions of the first and second harmonics $(\lambda_{if1}, \lambda_{if2})$. Note that the coefficients are a function of fuselage angle of attack also. The fit is based on data of the airfoiled part of the blade between $A = 0.25 \le r \le B = 0.97$ of Fig. 2 (b).

c_n, $n=$	0	1	2	3
$\lambda_{if\,0}$	0.0324	-0.1529	0.2061	-0.0866
λ_{if1}	0.1195	-0.1077	-0.1239	0.1245
λ_{if2}	0.0426	-0.2206	0.3124	-0.1356

Table 1: Polynomial coefficients of inflow distributions for $\alpha = 0°$; harmonics $0,1,2/rev; N = 3$.

Summing up the terms, the result using $A = 0.25$ as effective begin of the airfoiled section of the blade and $B = 0.97$ as the effective radius becomes:

$$\Delta C_T / \sigma = 1.3798\Theta_S \mu + 0.00293\mu \quad (1.10)$$

The CFD data indicate a strong dependency on fuselage angle of attack, such that within the range of α investigated this dependency can be represented by a polynomial of second order. Referenced to the nominal weight coefficient of $C_W / \sigma = 0.06286$ - which represents a 2.2 ton Bo105 scaled down to the model rotor - the increase of thrust due to the presence of a fuselage relative to the thrust of the isolated rotor is, including the dependency on α

$$\frac{\Delta C_T}{C_W} = \mu(21.95\Theta_S + 0.0466 - 1.196\alpha - 0.1957\alpha^2) \quad (1.11)$$

The change of thrust due to the fuselage will therefore be linear in flight speed and quadratic in α. Since the linear term in α is dominating there will be a strong thrust increase when the fuselage is tilted nose-down, as usually is the case in high speed flight. The reason is that most of the fuselage generates an upwash in the rotor disk. Only a small thrust increase is obtained for $\alpha = 0$ which means that the upwash and downwash is about in balance, while for nose-up attitudes there will be a reduction of thrust, compared to the isolated rotor. It must be noted that the fuselage lift or download acts just opposite to its influence on thrust. As long as the fuselage loads are unknown it is reasonable to assume that they are of equal size, i.e., the fuselage lift is cancelling the change of thrust. For trimming the flight this means the collective control of the isolated rotor has to be kept constant when the fuselage is included, but the hub moments have to be re-trimmed by the cyclic controls.

2.3. Impact on Trim Controls

Blade element theory can also be applied in estimating the influence of such a fuselage-induced velocity field on cyclic controls. In order to keep the hub moments the same, the blade motion must be the same with or without fuselage-induced velocities. For simplicity, assume zero flapping of an articulated blade, which must be restored using cyclic controls when a disturbance like the fuselage flow field generates 1/rev moments.

Fig. 2 (a) shows essentially a $1/rev$ variation of the fuselage-induced velocities with upwash in the front and downwash in the rear. For a rotating blade, this principally represents a $1/rev$ Cosine loading variation which - to maintain trim - must be opposed by the lateral control angle Θ_C. In addition, the asymmetry of dynamic pressure on advancing and retreating side will generate a $1/rev$ Sine component in the loading, which must be compensated by a longitudinal control angle Θ_S in order to maintain trim. The magnitude can be estimated from the individual blade loading, based on blade element theory like before. The aerodynamic flap moment about the hub center is investigated. Then, using *Eq. (1.5)* for the local contribution of the differential thrust to the flap moment becomes

$$M_\beta(\psi) = R^2 \int_A^B dT\, r\, dr = R^2 \frac{\rho}{2} (\Omega R)^2 c C_{l\alpha} \times$$
$$\int_A^B r \left[(r + \mu\sin\psi)^2 (\Theta_C \cos\psi + \Theta_S \sin\psi) - \mu(r + \mu\sin\psi)\lambda_{if}(r) \right] dr \quad (1.12)$$

The steady part affects the blade coning and represents the thrust increase as shown before. Since only the $1/rev$ flapping moment must be compensated by the cyclic controls in order to maintain moment trim, the steady part and all higher harmonic components $(n \ge 2)$ can be ignored.

Extracting the $1/rev$ components and dividing by $R^2(\rho/2)(\Omega R)^2 c C_{l\alpha}$ results in the non-dimensional flap moment of the $1/rev$ part, $\overline{M}_{\beta 1}$.

$$\bar{M}_{\beta 1}(\psi) = \cos\psi \int_A^B \left[\Theta_C \left(r^3 + r\frac{\mu^2}{2} - r\frac{\mu^2}{4} \right) - \mu r^2 \lambda_{if1}(r) \right] dr + \sin\psi \int_A^B \left[\Theta_S \left(r^3 + r\frac{\mu^2}{2} + r\frac{\mu^2}{4} \right) - \mu^2 r \lambda_{if0}(r) + \frac{\mu^2}{2} r \lambda_{if2}(r) \right] dr \quad (1.13)$$

Compensating the $1/rev$ of the moment by the cyclic controls means that both the terms of the Cosine and the Sine must individually be zero. This results in two equations where the integrals of the above are both set to zero since both $\cos\psi$ and $\sin\psi$ are non-zero. For the Cosine term we obtain:

$$0 = \int_A^B \left[\Theta_C \left(r^3 + r\frac{\mu^2}{4} \right) - \mu r^2 \lambda_{if1}(r) \right] dr$$

$$\Theta_C = \mu \frac{\sum_{n=0}^{N} c_{n1} \frac{B^{n+3} - A^{n+3}}{n+3}}{\frac{B^4 - A^4}{4} + \mu^2 \frac{B^2 - A^2}{8}} \quad (1.14)$$

and for the Sine term:

(1.15)

$$0 = \int_A^B \left[\Theta_S \left(r^3 + r\frac{3\mu^2}{4} \right) - \mu^2 r \lambda_{if0}(r) + \frac{\mu^2}{2} r \lambda_{if2}(r) \right] dr$$

$$\Theta_S = \mu^2 \frac{\sum_{n=0}^{N} \left(c_{n0} - \frac{c_{n2}}{2} \right) \frac{B^{n+2} - A^{n+2}}{n+2}}{\frac{B^4 - A^4}{4} + 3\mu^2 \frac{B^2 - A^2}{8}}$$

From all terms of the fuselage-induced velocities the only important terms in Eqs. (1.14) and (1.15) are those of $0, 1, 2/rev$. Similar to the steady part shown in Fig. 2 (b) the radial distribution of the $1/rev$ and $2/rev$ parts of the fuselage-induced velocity can be approximated by a polynomial. The coefficients are given in Table 1, and it can be seen that the $1/rev$ is significantly larger than the mean value or the $2/rev$ part, as Fig. 2 (b) also shows. Thus, the effect on $1/rev$ blade loading will be much stronger than on the mean or on the $2/rev$.

Like in the thrust investigation, the coefficients depend on the fuselage angle of attack, such that the sum in the nominators can be expressed as polynomial of second order in the fuselage angle of attack.

$$\Theta_C = \mu \frac{0.008 + 0.0112\alpha - 0.0194\alpha^2}{0.2203 + 0.1098\mu^2}$$

$$\Theta_S = \mu^2 \frac{-0.00009 + 0.0148\alpha - 0.0028\alpha^2}{0.2203 + 0.3294\mu^2} \quad (1.16)$$

In hover there is no effect on controls since the forward speed is zero and with it the fuselage-induced velocity field. Of course, in this case the fuselage is subjected to the rotor downwash from top and will block it similar to a ground effect, and this represents a fuselage angle of -90°, which is not addressed here.

The fuselage effect on Θ_C grows essentially linear in μ and quadratic in μ on Θ_S. This is expected since in the 0° and 180° azimuth position of the disk the flight speed does not contribute to the local dynamic pressure and the section angle of attack increase due to fuselage-induced downwash is linear with flight speed. At the $\psi = 90°$ and $270°$ azimuth positions the flight speed contributes to the blade section dynamic pressure and thus its squared value is found in the results for Θ_S.

3. DATA GENERATION USING CFD

3.1. CFD Code Description

A three-dimensional, structured, unsteady Reynolds-averaged Navier-Stokes (RANS) solver, called KFLOW [40], is used to obtain the flow field around the isolated fuselage. The *k*-ω Wilcox-Durbin (WD+) scheme is employed for the turbulence model [41]. For the spatial discretization, the inviscid fluxes are calculated using the fifth-order weighted essentially non-oscillatory scheme, while the central difference scheme is used for the viscous fluxes. A time accurate simulation is conducted using a second-order, dual-time stepping scheme for the temporal algorithm. The non-dimensional time step size used in the present time marching solution is $\Delta\psi = 0.2°$. The number of sub-iterations performed at each physical time step is set to 10. The no-slip boundary condition is applied at the solid wall of the fuselage surface.

3.2. HART II Fuselage Data Generation

Fig. 3 shows the inner part of the computational grid created using the O-mesh topology for the HART II fuselage configuration along with the Cartesian background grid system. The near-body fuselage grid consists of about 2.5 million cells while the background off-body grid amounts to 29 million cells, overall leading to about 31.5 million cells.

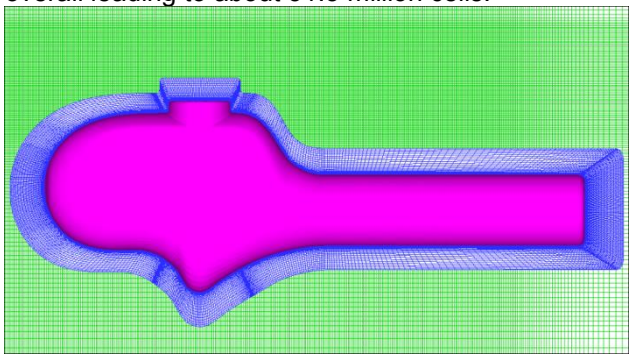

Fig. 3: Computational grids for the fuselage.

The background grid has a uniform spacing of 10% chord length ($0.1c$). The cell spacing for the first grid point from the wall boundary is set to $1.0\text{x}10^{-5}c$ to resolve the viscous sub-layer in the turbulent boundary layer. The computation is made using a Linux-based PC cluster system with 2.93 GHz Intel I7-870 processors. All runs use a total of 80 processors.

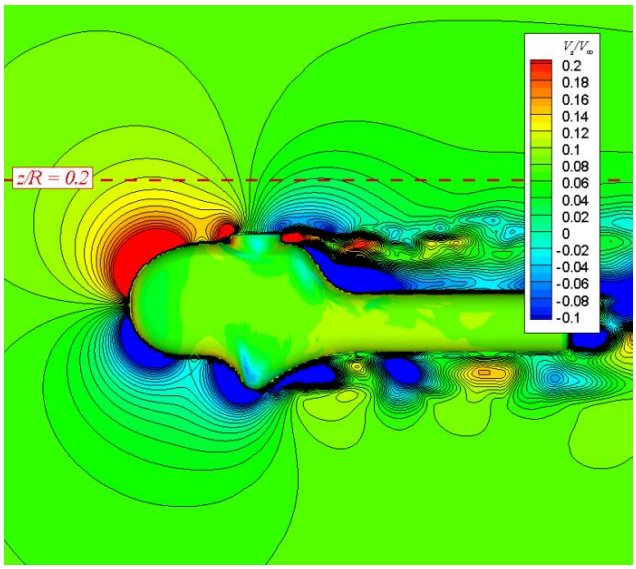

(a) Lateral view, plane $y/R = 0$

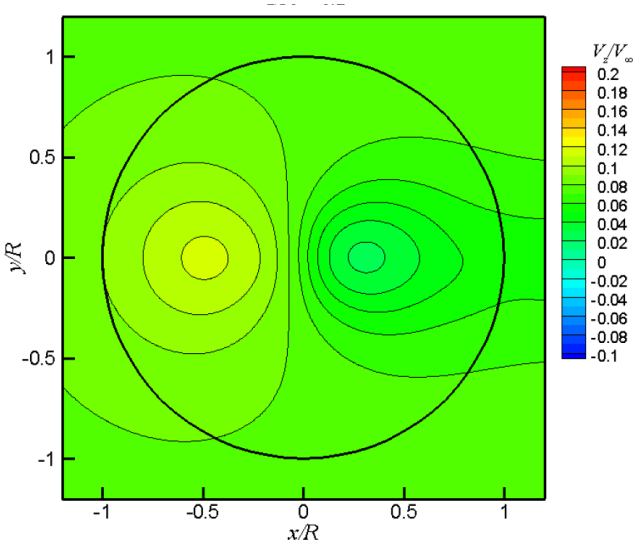

(b) Top view, plane $z/R = 0.2$

Fig. 4: Induced vertical velocity field of the HART II fuselage for $\alpha = 0°$.

Numerical simulations are performed to obtain the flow field around the isolated HART II fuselage at different shaft tilt angles in low speed forward flight. A total of 7200 time steps (corresponding to four rotor revolutions) are computed to reach a steady flow characteristic and the last 450 time step data are averaged to be processed for further analysis. Fig. 4 (a) shows the contour plot for the fuselage-induced vertical velocity component, non-dimensionalized by the free stream velocity V_∞, along the longitudinal cut plane ($y/R = 0$) when the shaft angle α is zero.

As is depicted, the flow field is quite monotonic over the front fuselage region while the unsteadiness of the flow is dominant aft of the hub toward the empennage region, despite the fact that the velocity components are averaged. It is demonstrated also in Fig. 4 (b), depicting the induced velocity at $z/R = 0.2$ located above the hub center, that the upwash in the front and the downwash in the rear of the hub center are clearly captured.

4. MODELING OF INDUCED VELOCITIES

The vertical velocity component of the CFD data was extracted in four planes parallel to the rotor disk. Using the non-linear least-squares method, a three-dimensional semi-empirical, physics-based analytical model consisting of polynomial and rational equations is fitted to the velocity field. The fit is calculated for all four planes separately first and concluded with a second fit between the planes. This allows the analytical representation of the CFD data within the entire volume surrounding the rotor with high accuracy, but minimum computational effort, such as required in comprehensive codes.

4.1. Data Analysis, Physical Understanding

Results from the CFD computation are shown in Fig. 4 (a) for the plane $y/R = 0$ and in Fig. 4 (b) for the plane $z/R = 0.2$. There are two distinct features: an upwash in the front and a downwash in the rear of the disk, both with a maximum on the centerline due to lateral symmetry of the body. A cut along the longitudinal axis at $y/R = 0$ is shown in Fig. 5 (a) and a cut across the front and rear maxima, normalized by the respective maximum values, is shown in Fig. 5 (b). This fundamental behavior is present in each of the planes $z/R = -0.1$, 0, 0.1 and 0.2, with increasing maximum values when approaching the fuselage.

The planes $z/R = 0$ and -0.1 also include turbulent flow due to separation behind the hub fairing. The extent of such separation depends on the shaft angle. Positive angles will affect the planes $z/R = 0.1$ and 0.2 as well, while negative angles will affect the plane $z/R = -0.1$ and below. A fully time-averaged data set would show smooth and continuous data and no turbulent structures. Since the purpose of the mathematical representation is to compute only the mean values the identification of

function parameters must take care of ignoring the turbulent structures by means of clipping or lower weight for the data contained therein.

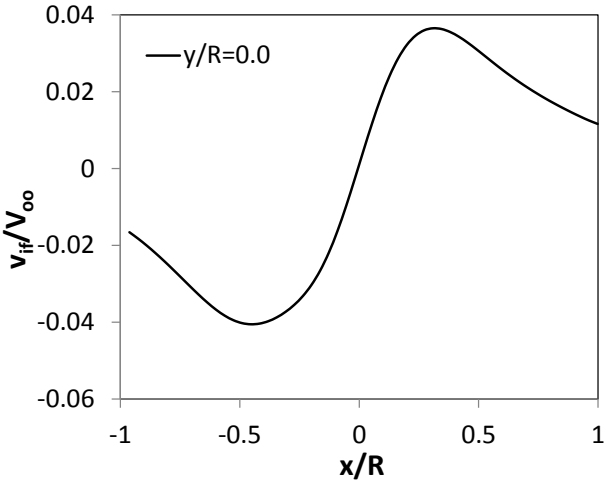

(a) Longitudinal cut through the centerline

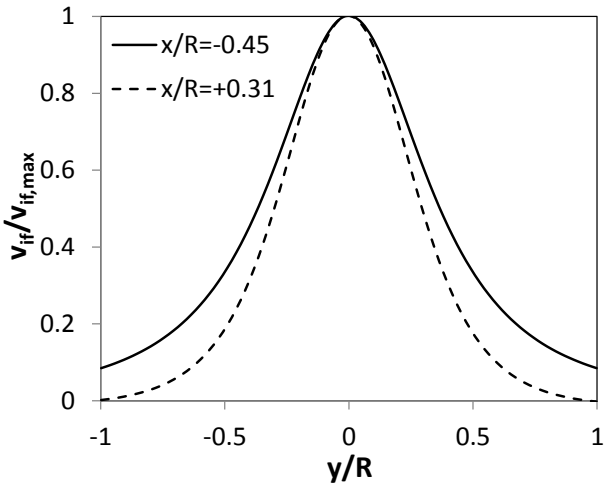

(b) Lateral cut through the front and rear maxima

Fig. 5: Induced vertical velocity profiles along cuts through Fig. 4 (b), $z/R = +0.2$.

The goal is to represent the data by means of simple analytical formulae, which requires the selection of a suitable coordinate system. Since the fuselage influence as shown in Fig. 4 (b) is periodic for the revolving blade a truncated Fourier series may be suggested for the azimuthal representation and a polynomial for the radial shape functions.

However, the model should also be usable in a simple manner for the wake convection. This requires a Cartesian coordinate system. Since the conversion from polar coordinates to Cartesian results in quite complicated expressions that may be difficult to integrate analytically the choice is made to use Cartesian coordinates.

4.2. Definition of Formula

The distribution of velocities shown in Fig. 5 (a) suggests representing each feature visible by a separate function. The upwash area in the front will get one function that has its maximum where the data has it, and the function has to vanish to all sides: to the front and rear as seen in the profile of Fig. 5 (a), but also to the sides as seen in Fig. 5 (b). In the same way the downwash area in the rear has to be treated and possibly the influence of a tail boom as well, which might be visible for $x/R > 0.5$.

The separation of variables also suggests to model the shape function separately from the peak value, such that after dividing by the peak value the shape function has a maximum of 1, as shown for the lateral profile in Fig. 5 (b). It must be expected that the shape of the individual function may change in dependence on the proximity to the fuselage, z/R, as does the peak value, which is shown in Fig. 6. For large distances above the fuselage the peak value approaches zero, as must be the case for large distances below the fuselage.

A generic function to describe each of the individual upwash and downwash shapes in x, y and z, fulfilling the condition to vanish for large values of the respective parameter, is found in the following formula:

$$
\begin{aligned}
v_i(x,y,z) &= S_A(z) * S_x(x,z) * S_y(y,z) \\
S_A(z) &= A_0 \frac{1}{f_A(z-z_0)^2 + 1} \\
S_x(x,z) &= \frac{1}{f_x(z)(x-x_0)^2 + 1} \\
S_y(y,z) &= \frac{1}{f_y(z)y^2 + 1}
\end{aligned}
\tag{1.17}
$$

For every individual phenomenon observed one of this set of functions has to be employed, as there are: (a) the upwash in the front of the disk, (b) the downwash in the rear, (c) an upwash (or downwash, depending on shaft angle of attack) caused by the tail boom, where the maximum influence can be fixed to $x/R = 1$. The latter can be seen as well in Fig. 2 (a) and Fig. 4 (b) in the area $x/R > 0.7$ and $-0.5 < y/R < +0.5$ in form of a downwash extending to the end of the disk.

x_0 represents the x/R position of the peak velocity. However, this contribution usually is small and may be ignored as long as it does not significantly contribute to the distribution of induced velocities. z_0 may be set as the fuselage center and the curve shown in Fig. 6 may be seen as part of the curve shown in Fig. 5 (b).

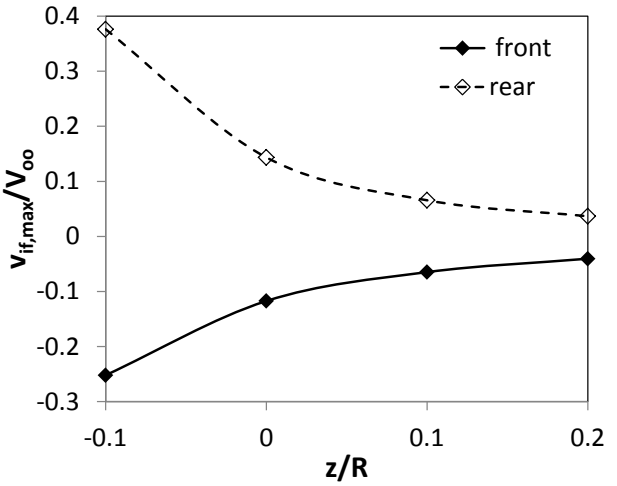

Fig. 6: Maximum induced vertical velocity of the upwash and the downwash as function of the distance to the fuselage.

All of the functions S have the form of a bell curve like that shown in Fig. 5 (b) and the parameter f therein defines its shape. As it approaches zero, $S \to 1$ independent of the coordinate x, y or z with which it is multiplied. For very large values of f the shape function $S \to 0$ except for $x = x_0$, $z = z_0$, or $y = 0$, in which cases $S = 1$. For all intermediate values of f a bell-like curve is obtained with a width depending on the value of f.

4.3. Identification of Parameters

Initially, all parameters of the set of functions in each plane were identified independently. Thus, the dependence on z/R must not yet be included, which reduced the number of parameters to the following set of 11 for every individual z/R plane:

(a) upwash in the front: $A_{0f}, f_{xf}, x_{0f}, f_{yf}$
(b) downwash in the rear: $A_{0r}, f_{xr}, x_{0r}, f_{yr}$
(c) tailboom in the rear: A_{0t}, f_{xt}, f_{yt}

A best fit to the CFD data was obtained using a multi-variable optimizer, based on the sum of squared errors to be minimized. Only the data within the rotor disk were used and for the planes $z/R = -0.1$ and 0 the root cutout region of $0.22R$ was ignored, as were the turbulent zones downstream of the hub fairing where they affected the flow field.

The second step was to analyze the variation of optimized parameters with respect to the z/R coordinate. It was found that the shape function parameters f and the peak values A_0 all had a variation like the one shown in Fig. 6, while the x/R position did not change and could be set as a constant. Therefore, f_x, f_y can be modeled similar to $S_A(z)$ as

$$f_x(z) = A_{xz} \frac{1}{f_{xz}(z - z_0)^2 + 1}$$
$$f_y(z) = A_{yz} \frac{1}{f_{yz}(z - z_0)^2 + 1} \quad (1.18)$$

This adds 3 parameters to each of the upwash, downwash and tail boom functions, totaling to 9 additional parameters. It allows a fully analytical representation of the vertical induced velocity in the entire volume, not only in the planes of identification without interpolation. All this was performed for the different shaft angle settings individually.

The final step then was looking for the dependencies of each individual parameter with respect to the shaft angle. Here it was found that all the shape function parameters f, x_0, z_0 did not depend on shaft angle (at least not in the range available: $-10° < \alpha < +10°$).

All the A_0 and x_0 showed a linear dependence. When the shaft angle increased, the upwash peak location in the front of the disk moved more towards the fuselage nose and the peak value became less than for $\alpha = 0°$. With $-10°$ nose down tilt the peak value increased and its position moved towards the hub center.

The downwash peak in the rear of the disk showed opposite behavior: for $+10°$ angle it had the largest peak value and its location moved more downstream while the peak value was the lowest for $-10°$ and its position moved a little towards the hub center.

An extreme position might be seen at $\alpha = -90°$, which aerodynamically represents a fuselage in hover or vertical climb, subjected to the induced velocity caused by rotor thrust that impinges from top onto the fuselage. In this special case all three fuselage components generate an upwash since every element blocks the flow.

The remaining errors were less than 10% of the maximum induced velocities found in every plane z/R.

4.4. Implementation into S4

The final model of the fuselage-induced velocities is implemented in the rotor simulation program S4 for the calculation of the rotor aerodynamics. To assess the validity of the newly implemented model, a series of simulations is carried out for the HART II model in descending and forward flight conditions.

5. MODELING OF WAKE DISTORTIONS

Within the prescribed-wake code of the rotor simulation program S4, the distortions of the wake are calculated analytically. The starting points x_s, y_s of root and tip vortices are delivered by the on-blade evaluation of the lifting-line method. The vortex filaments convect downstream with the free stream velocity V_∞ and experience a vertical displacement due to the induced velocity fields of the rotor and the fuselage. Convection in the lateral direction can be regarded as negligible. Since the fuselage flow field is superimposed on the other induced velocities affecting the wake geometry, its impact on wake perturbations can easily be separated.

The vertical location of a vortex filament z_v at a specific position x, y within or behind the rotor plane is therefore composed of the rotor-induced (z_R) and the fuselage-induced (z_F) displacements:

$$z_v(x,y) = z_R(x,y) + z_F(x,y,z) \tag{2.19}$$

The dependency $z_F = f(z)$ requires the integration of the fuselage-induced velocity field v_i along the initially unknown vortex trajectory z_v. The necessary numerical or stepwise analytical integration would lead to increased computational costs. Therefore, a simplified approach based on analytical integration along x with $z = const$ was realized here:

$$z_F(x,y,z) = \int_{x_s}^{x} v_i(x,y,z)dx \tag{2.20}$$

$$= S_A(z) * S_y(y,z) * \int_{x_s}^{x} S_x(x,z)dx$$

$$= A_0 \frac{1}{f_A(z-z_0)^2+1} * \frac{1}{f_y(z)y^2+1}$$

$$* \left[\frac{\tan^{-1}\left(\sqrt{f_x}\,(x-x_0)\right)}{\sqrt{f_x}} - \frac{\tan^{-1}\left(\sqrt{f_x}\,(x_s-x_0)\right)}{\sqrt{f_x}} \right]$$

In Fig. 7, a comparison of the analytically and the stepwise analytically integrated fuselage-induced velocity field is shown.

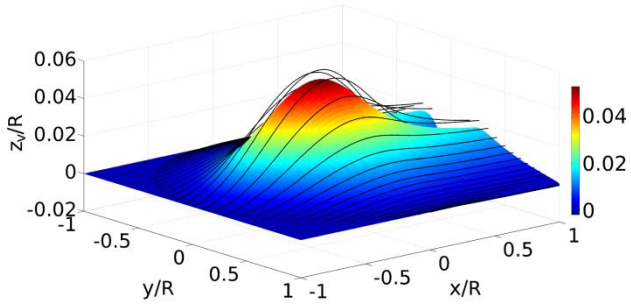

Fig. 7: Comparison of analytically (colored surface) and stepwise analytically (black lines) integrated wake geometries.

The analytically integrated displacement field is depicted as a colored surface and was calculated using Eq. (2.20) with a constant and conservative value of $z/R = 0.05$, which corresponds to a typical height of the tip path plane. The black lines represent the stepwise analytically integrated displacement field, which was calculated using a step size of $\Delta x/R = 0.01$ and stepwise adapted z/R. The maximum deviation between both methods is below 10% of z_F. Because of this relatively large loss of accuracy, the analytical integration can only be considered a preliminary solution that has to be improved in future studies.

6. RESULTS AND DISCUSSION

6.1. Analytical Results

In Fig. 8, the fuselage-induced velocity field given by the analytical regression model is plotted for four planes $z/R = -0.1, 0, 0.1, 0.2$. The dominant features of the flow field are visualized in the plot, e.g. the induced up- and downwash in front and behind the hub center, as well as the asymptotic decline of the velocity with increasing distance to the fuselage center. The maximum deviation of the analytical model from the reference data was found to be less than 5% of the maximum induced velocity and less than 2.5% of the inflow velocity V_∞, respectively.

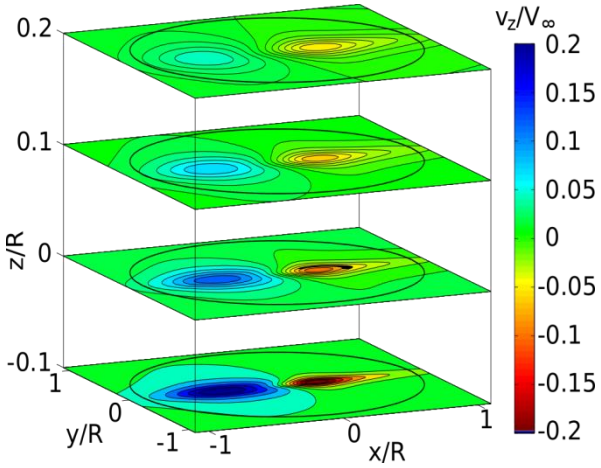

Fig. 8: Fuselage-induced velocity field from the analytical regression model, plotted in four horizontal cut planes. Incoming flow from the left; rotor circumference is indicated by the black circle.

6.2. S4 Results

The total induced velocity fields of a trimmed rotor in forward flight at $V_\infty = 50$ m/s are shown without the influence of the HART II fuselage in Fig. 9 (a) and with it in Fig. 9 (b). The impact of the fuselage-induced flow is mainly visible along the centerline of the helicopter model, where in the front – upstream of the rotor center – an upwash is visible and behind the rotor center a downwash is caused by the

fuselage. Since the rotor blades are having a steady coning due to thrust they typically operate at a level about $z/R = 0.05$ above the hub center. For simplicity, the fuselage-induced velocities are computed here for this plane only, but there is no general limitation to account for the individual blade element elevation instead.

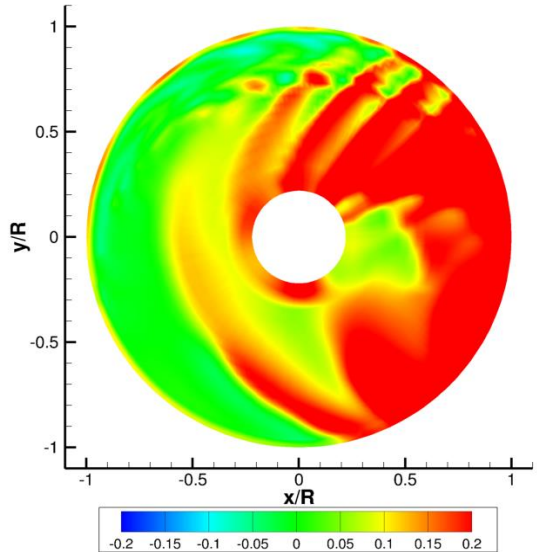

(a) isolated rotor without fuselage

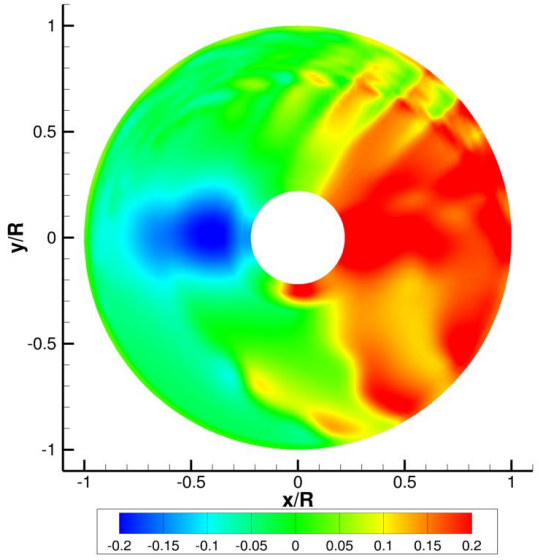

(b) with fuselage-induced velocities

Fig. 9: Induced velocity field v_z/V_∞ in the plane of the rotor at $V_\infty = 50$ m/s for the same rotor thrust.

6.3. Nonlinear Trim: Comparison with Theory

To verify the theoretical results derived in Sect. 2 DLR's comprehensive rotor code S4 is run using the Bo105 model rotor with just the first flapping degree of freedom. The isolated rotor computations were first performed for $\alpha = -10°, 0°, +10°$ using a trim to constant thrust and zero hub moments throughout the range of $0 \le \mu \le 0.5$. Then, the respective collective control was kept fixed, the fuselage influence included and the hub moments re-trimmed to zero using cyclic controls only (curves denoted "fus+coll").

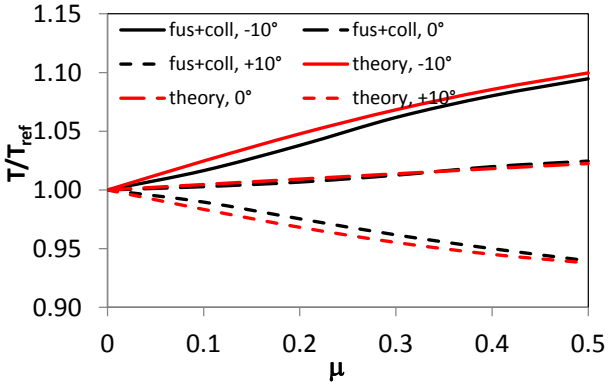

(a) Relative change of thrust due to fuselage effect

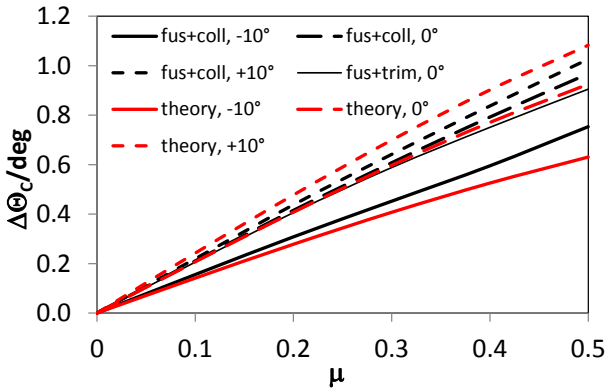

(b) Relative change of lateral cyclic

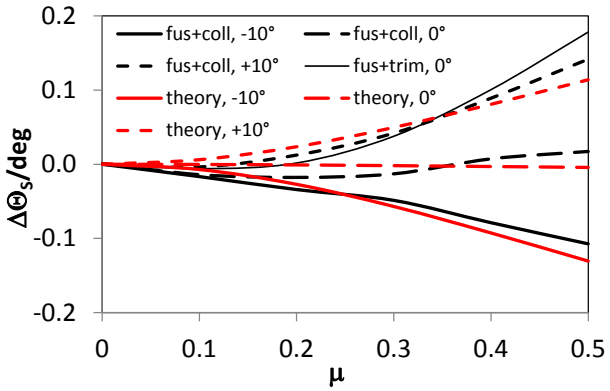

(c) Relative change of longitudinal cyclic

Fig. 10: Fuselage effect on thrust and cyclic controls.

This provides the changes in thrust and power, as well as in the cyclic controls to maintain the moment trim. In addition, for $\alpha = 0°$ the thrust was also re-trimmed, which provides the change in collective required to keep the thrust constant (curve "fus+trim").

The results of the fully non-linear simulation (including unsteady aerodynamics, compressibility effects, stall, reversed flow, locally yawed flow effects and using a global downwash model of Mangler and Squire for the general inflow caused by the thrust) are given in Fig. 10. Despite the simplicity of the analytical model – including the ignorance of compressibility, stalled areas, reversed flow and others – the overall effects are correctly predicted, even in the range of high advance ratios.

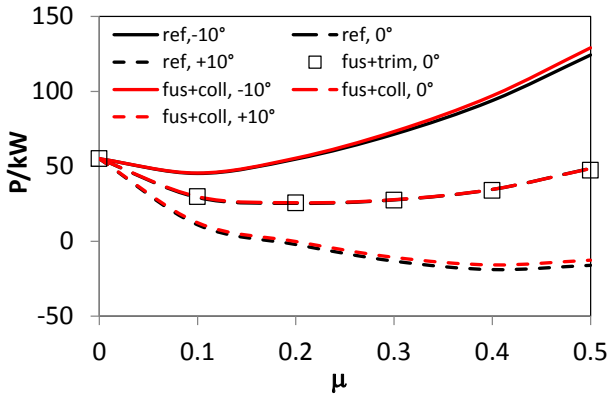

(a) Power without and with fuselage effect

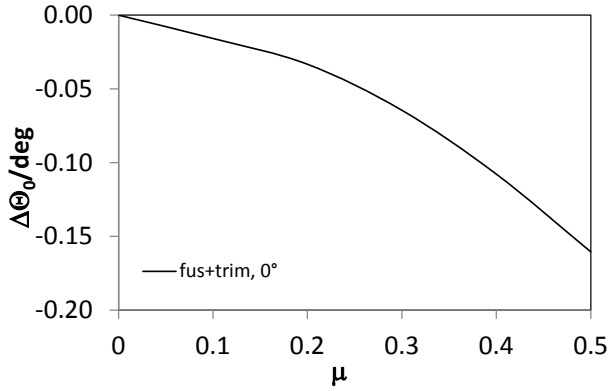

(b) Change of collective to compensate thrust increase for $\alpha = 0°$

Fig. 11: Fuselage effect on power and collective control.

The impact on power required, together with the change of collective that is required to re-trim to the thrust of the isolated rotor as well, is shown in Fig. 11. In general the changes in power are small compared to the reference power computed by the isolated rotor. This means whenever the thrust is increased due to the fuselage-induced velocities the power increase due to thrust increase is compensated by the "ground effect" of the fuselage. When the thrust increase is compensated by re-trimming to the reference thrust this requires a change of collective to compensate the mean upwash or downwash. In Fig. 11 (b) this is shown for $\alpha = 0°$, where a slight thrust increase is observed in Fig. 10 (a) when the collective is kept fixed from the isolated rotor computation. To compensate for this increase in thrust the collective has to be gradually reduced.

7. FURTHER ANALYSIS

The generic formulation used here is applicable within any comprehensive rotor code and also for any kind of fuselage. The application is two-fold: first within the blade section local aerodynamics and second within either prescribed or free-wake codes to compute additional wake geometry perturbations caused by the fuselage presence. The modified wake geometry will also cause some differences in the wake-induced velocities at the rotor. The impact on rotor thrust and controls to maintain rotor trim for balanced moments can be estimated analytically. It will be shown that in fast forward flight the fuselage-induced velocities will cause about 8% increase in rotor thrust and about $1°$ in lateral cyclic control Θ_C, compared to the isolated rotor. These analytic results are validated by a fully non-linear simulation using DLR's S4 rotor code.

8. CONCLUSIONS

The method proposed here is a simple enhancement for comprehensive codes for inclusion of mutual effects between fuselage and rotor. Here, the focus is placed on fuselage-rotor interference but it must be understood that accounting for this effect must be accompanied by also accounting for the effect of the rotor on the fuselage causing an additional download.

It is found that the fuselage represents an equivalent to a ground effect and locally modifies the flow direction within the rotor disk. The mean influence can be thrust increasing or decreasing, depending on the fuselage angle of attack.

The use of Cartesian coordinates and simple functions for the mean induced effects allows the analytic computation of the fuselage-induced velocities in the entire volume of the rotor disk:

(a) on the blade elements at any azimuthal, radial and vertical position
(b) on any vortex element within this volume, be it prescribed wake or free-wake.

The first item is important for the section airloads and a large additional fuselage-induced angle of attack may cause premature stall on the blades. This cannot be computed if an isolated rotor is investigated without a fuselage. The second item is important for the wake geometry and the vortex convection.

References

AHS = American Helicopter Society International
AHSF = AHS Annual Forum and Technology Display
JAHS = Journal of the AHS

[1] Sheridan, P.F., Smith, R.P.: *Interactional Aerodynamics – a New Challenge to Helicopter Technology*, JAHS **25** (1), 3-21, 1980

[2] Huber, H., Polz, G.: Studies on Blade-to-Blade and Rotor-Fuselage-Tail Interferences, Aircraft Engineering and Aerospace Technology **55** (10), 2 – 12, 1983

[3] Keys, C., Wiesner, R.: *Guidelines for Reducing Helicopter Parasite Drag*, JAHS **20** (1), 31-40, 1975

[4] Leishman, J.G., Bi, N.: *Aerodynamic Interactions Between a Rotor and a Fuselage in Forward Flight*, JAHS **35** (3), 22-31, 1990

[5] Bi, N., Leishman, G.: *Experimental Study of Rotor/Body Aerodynamic Interactions*, AIAA Journal of Aircraft **27** (9), 779-788, 1990

[6] McVeigh, M.A., Grauer, W.K., Paisley, D.J.: *Rotor/Airframe Interactions on Tiltrotor Aircraft*, JAHS **35** (3), 43-51, 1990

[7] Bagai, A., Leishman, J.G.: *Experimental Study of Rotor Wake/Body Interactions in Hover*, JAHS **37** (4), 48-57, 1992

[8] Betzina, M.D., Smith, C.A., Shinoda, P.: *Rotor/Body Aerodynamic Interactions*, VERTICA **9** (1), 65-81, 1985

[9] Smith, C.A., Betzina, M.D.: *Aerodynamic Loads Induced by a Rotor on a Body of Revolution*, JAHS **31** (1), 29-36, 1986

[10] Le Pape, A., Gatard, J., Monnier, J.-C.: *Experimental Investigations of Rotor–Fuselage Aerodynamic Interactions*, JAHS **52** (2), 99-109, 2007

[11] Crouse, G.L., Leishman, G.J., Bi, N.: *Theoretical and Experimental Study of Unsteady Rotor/Body Aerodynamic Interactions*, JAHS **37** (1), 55-65, 1992

[12] Berry, J., Bettschart, N.: *Rotor/Fuselage Interaction: Analysis and Validation with Experiment*, 53rd AHSF, Virginia Beach, VA, April 29-May 1, 1997

[13] Wilby, P.G., Young, C., Grant, J.: *An Investigation of the Influence of Fuselage Flow Field on Rotor Loads and the Effects of Vehicle Configuration*, VERTICA **3** (2), 79-94, 1979

[14] Rand, O.: *Influence of Interactional Aerodynamics on Helicopter Rotor/Fuselage Coupled Response in Hover and Forward Flight*, JAHS **34** (4), 28-36, 1989

[15] Rand, O., Gessow, A.: *Model for Investigation of Helicopter Fuselage Influence on Rotor Flowfields*, AIAA Journal of Aircraft **26** (5), 401-402, 1989

[16] Mavris, D.N., Komerath, N.M., McMalhon, H.M.: *Prediction of Aerodynamic Rotor-Airframe Interactions in Forward Flight*, JAHS **34** (4), 37-46, 1989

[17] Schillings, J., Reinesch, R.: *The Effect of Airframe Aerodynamics on V-22 Rotor Loads*, JAHS **34** (1), 26-33, 1989

[18] Lorber, P.F., Egolf, T.A.: *An Unsteady Helicopter Rotor-Fuselage Aerodynamic Interaction Analysis*, JAHS **35** (3), 32-42, 1990

[19] Crouse, G.L.: Active *Control of Vibratory Airloads Induced by Helicopter Rotor-Fuselage Interactions*, AIAA-93-1363-CP, AIAA/ASME/ASCE/AHS/ASC 34th Structures, Structural Dynamics, and Materials Conference, La Jolla, CA, April 19-21, 1993

[20] Quackenbush, T.R., Lam, C.-M.G., Bliss, D.B.: *Vortex Methods for the Computational Analysis of Rotor/Body Interaction*, JAHS **39** (4), 14-24, 1994

[21] Wachspress, D.A., Quackenbush, T.R., Boschitsch, A.H.: *Rotorcraft Interactional Aerodynamics with Fast Vortex/Fast Panel Methods*, JAHS **48** (4), 223-235, 2003

[22] Kenyon, A.R., Brown, R.E.: *Wake Dynamics and Rotor–Fuselage Aerodynamic Interactions*, JAHS **54** (1), 012003-1 – 012003-18, 2009

[23] Kelly, M. E., Brown, R.E.: *The Effect of Blade Aerodynamic Modeling on the Prediction of the Blade Airloads and the Acoustic Signature of the HART II Rotor*, 35th European Rotorcraft Forum, Hamburg, Germany, Sept. 22-25, 2009

[24] Nam, H.J., Park, Y.M., Kwon, O.J.: *Simulation of Unsteady Rotor–Fuselage Aerodynamic Interaction Using Unstructured Adaptive Meshes*, JAHS **51** (2), 141-149, 2006

[25] Renaud, T., O'Brien, D., Smith, M., Potsdam, M.: *Evaluation of Isolated Fuselage and Rotor-Fuselage Interaction Using Computational Fluid Dynamics*, JAHS **53** (1), 3-17, 2008

[26] Wagner, S., Dietz, M., Embacher, M*.: Influence of Grid Arrangements and Fuselage on the Numerical Simulation of the Helicopter Aeromechanics in Slow Descent Flight*, 15th International Conference on Computational & Experimental Engineering and Sciences Conference (ICCES08), Honolulu, HI, March 17-22, 2008

[27] Lim, J.W., Dimanlig, A.C.B.: *An Investigation of the Fuselage Effect for HART II Using a CFD/CSD Coupled Analysis*, 2nd International Forum on Rotorcraft Multidisciplinary Technology, Seoul, Korea, Oct. 19-20, 2009

[28] Lim, J.W., Dimanlig, A.C.B.: *The Effect of Fuselage and Rotor Hub on Blade-Vortex Interaction Airloads and Rotor Wakes*, 36th European Rotorcraft Forum, Paris, France, Sept. 7-9, 2010

[29] Sa, J.H., Kim, J.W., Park, S.H., You, Y.-H., Park, J.-S., Jung, S.N., Yu, Y.H.: *Prediction of HART II Airloads Considering Fuselage Effect and Elastic Blade Deformation*, 4th AHS International Meeting on Advanced Rotorcraft Technology and Safety Operations (Heli Japan), Saitama, Japan, Nov. 1-3, 2010

[30] Sa, J.H., You, Y.-H., Park, J.-S., Jung, S.N., Park, S.H., Yu, Y.H.: *Assessment of CFD/CSD Coupled Aeroelastic Analysis Solution for HART II Rotor Incorporating Fuselage Effects*, 67th AHSF, Virginia Beach, VA, May 3-5, 2011

[31] Park, J.-S., Sa, J.-H., You, Y.-H., Jung, S.N., Park, S.-H.: *Fuselage Effect in Multibody Dynamics/CFD Coupled Analysis for a Rotor Correlation in Descending Flight*, 1st Asian Australian Rotorcraft Forum and Exhibition, Busan, Korea, Feb. 12-15, 2012

[32] Lim, J.W., Wissink, A., Jayaraman, B., Dimanlig, A.: *Helios Adaptive Mesh Refinement for HART II Rotor Wake Simulations*, 68th AHSF, Ft. Worth, TX, May 1-3, 2012

[33] Biava, M., Vivegano, L.: *Simulation of a complete helicopter: A CFD approach to the study of interference effects*, Aerospace Science and Technology **19** (1), 37-49, 2012

[34] van der Wall, B.G.: *Extensions of Prescribed Wake Modeling for Helicopter Rotor BVI Noise Investigations*, CEAS Aeronautical Journal **3** (1), 93-115, 2012

[35] Stepniewski, W.Z., Keys, C.N., *Rotary-Wing Aerodynamics*, ISBN 0486646475, Dover Publications, 1984

[36] Dreier, M.E.: *Introduction to Helicopter and Tiltrotor Flight Simulation*, ISBN-13: 978-1-56347-873-4, AIAA Education Series, Reston, VA, 2007

[37] van der Wall, B.G., *Analytic Formulation of Unsteady Profile Aerodynamics and its Application to Simulation of Rotors*, ESA-TT-1244, 1992 (Translation of DLR-FB 90-28, 1990)

[38] van der Wall, B.G., Lim, J.W., Smith, M.J., Jung, S.N., Bailly, J., Baeder, J.D., Boyd, D.D., *An Assessment of Comprehensive Code Prediction State-of-the-Art Using the HART II International Workshop Data*, 68th AHSF, Ft. Worth, TX, USA, May 1-3, 2012

[39] Göpel, C., van der Wall, B.G., *Über den Einfluß der Rotorversuchsstände ROTEST und ROTOS auf die Rotordurchströmung im DNW* (About the Influence of the Rotor Test Rigs ROTEST and ROTOS on the Flow in the Rotor Disk in DNW), DLR Mitt. 91-16, 1991

[40] Kim, J.W., Park, S.H., Yu, Y.H., *Euler and Navier-Stokes Simulations of Helicopter Rotor Blade in Forward Flight Using an Overlapped Grid Solver*, AIAA 2009-4268, 19th AIAA CFD Conference, San Antonio, TX, USA, June 22-25, 2009

[41] Park, S.H., Kwon, J.H., *Implementation of k-ω Turbulence Models in an Implicit Multigrid Method*, AIAA Journal, **42** (7):1348-1357, 2004

[42] van der Wall, B.G., *A Comprehensive Rotary-Wing Database for Code Validation: The HART II International Workshop*, The Aeronautical Journal of the Royal Aeronautical Society, **115** (1163), Jan. 2011, pp. 91-102; erratum in: **115** (1166), April 2011, p. 220